Constraining Global Marine Iron Sources and Ligand-Mediated Scavenging Fluxes With GEOTRACES Dissolved Iron Measurements in an Ocean Biogeochemical Model

Christopher J. Somes[1] , Andrew W. Dale[1] , Klaus Wallmann[1], Florian Scholz[1], Wanxuan Yao[1] , Andreas Oschlies[1] , Juan Muglia[2], Andreas Schmittner[3] , and Eric P. Achterberg[1]

[1]GEOMAR Helmholtz Centre for Ocean Research Kiel, Kiel, Germany, [2]Centro para el Estudio de los Sistemas Marinos, CONICET, Puerto Madryn, Argentina, [3]College of Earth, Ocean, and Atmospheric Sciences, Oregon State University, Corvallis, OR, USA

Abstract Iron is a key micronutrient controlling phytoplankton growth in vast regions of the global ocean. Despite its importance, uncertainties remain high regarding external iron source fluxes and internal cycling on a global scale. In this study, we used a global dissolved iron data set, including GEOTRACES measurements, to constrain source and scavenging fluxes in the marine iron component of a global ocean biogeochemical model. Our model simulations tested three key uncertainties: source inputs of atmospheric soluble iron deposition (varying from 1.4 to 3.4 Gmol/yr), reductive sedimentary iron release (14–117 Gmol/yr), and compared a variable ligand parameterization to a constant distribution. In each simulation, scavenging rates were tuned to reproduce the observed global mean iron inventory for consistency. The variable ligand parameterization improved the global model-data misfit the most, suggesting that heterotrophic bacteria are an important source of ligands to the ocean. Model simulations containing high source fluxes of atmospheric soluble iron deposition (3.4 Gmol/yr) and reductive sedimentary iron release (114 Gmol/yr) further improved the model most notably in the surface ocean. High scavenging rates were then required to maintain the iron inventory resulting in relatively short surface and global ocean residence times of 0.83 and 7.5 years, respectively. The model simulates a tight spatial coupling between source inputs and scavenging rates, which may be too strong due to underrepresented ligands near source inputs, contributing to large uncertainties when constraining individual fluxes with dissolved iron concentrations. Model biases remain high and are discussed to help improve global marine iron cycle models.

1. Introduction

Iron is a critical micronutrient limiting primary productivity in vast ocean regions (Boyd & Ellwood, 2010; Tagliabue et al., 2017). Iron limitation is responsible for the development of so-called High Nitrate Low Chlorophyll regions of the Southern Ocean, Subarctic North Pacific, Subarctic North Atlantic, and Eastern Equatorial Pacific (Moore et al., 2013). Since dissolved iron (DFe) in the ocean exists in the picomolar (pM) to nanomolar (nM) concentration range, historical measurements with higher detection limits and contamination issues have hindered a robust global understanding of the marine iron cycle compared to macronutrients (Bruland et al., 2014). However, over the past two decades, in large part due to the GEOTRACES program, considerable progress has been made and reliable intercomparable iron measurements have become available that permit a more synoptic view of the global marine iron cycle (Schlitzer et al., 2018).

The increasing number of robust iron measurements has sparked recent modeling efforts. However, few observational constraints are provided on a global scale, and the degree of complexity and assumptions on the mechanistic processes implemented in global marine iron models have varied dramatically (e.g., Tagliabue et al., 2016). For example, there is no consensus on the rates of key source fluxes to the ocean, particularly from atmospheric deposition (Anderson et al., 2016) and sedimentary release (e.g., Dale et al., 2015; Elrod et al., 2004) that vary between 1.4–30 Gmol yr^{-1} and 0–194 Gmol yr^{-1}, respectively, in state-of-the-art marine iron models (Tagliabue et al., 2016). Since uncertainties associated with scavenging and removal of DFe are also high, global marine iron models can tune scavenging rates to reproduce the global iron inventory with large ranges of sources fluxes (Frants et al., 2016; Pasquier & Holzer, 2017).

Another key aspect of marine iron models is the representation of ligands that organically bind DFe and thereby prevent it from being scavenged to sinking particulates. Some models still prescribe a globally constant ligand concentration typically at 1 nM, while others account for ligand distributions via a parameterization or directly simulating ligands as a prognostic tracer. Ligands are thought to be produced by microbes as a by-product during the production of organic matter (Gledhill & Buck, 2012), including by heterotrophic siderophores that flourish when systems become iron stressed (Bundy et al., 2018). This has led modelers to predict ligand concentrations by assuming they are produced during the production of organic matter (e.g., Völker & Tagliabue, 2015) or by prescribing a relationship to other organic tracers such as dissolved organic matter (DOM) and apparent oxygen utilization (AOU) (e.g., Misumi et al., 2013; Pham & Ito, 2018; Tagliabue & Völker, 2011).

The uncertainties associated with external source fluxes and scavenging represent key gaps in understanding the global marine iron cycle. This hampers accurate estimates of the DFe budget, residence time and, consequently, its sensitivity to environmental perturbations and climate change. While the rapidly increasing amount of DFe measurements is improving our knowledge of the distribution and inventory of dissolved iron in the ocean, constraining external fluxes has proved to be more difficult. As a result, the range of residence times estimated by the current global marine iron cycle models ranges from less than a decade to multiple centuries (Tagliabue et al., 2016), which limits our ability to confidently predict the impact of changes to the marine iron cycle on productivity in a future ocean. Observational estimates fall within a similar range (Johnson et al., 1997), noting that more recent studies estimate much shorter residence times in the upper ocean (~10 days–4 years) (Croot et al., 2004; Sarthou et al., 2003) depending on the local dynamics, iron pools considered, and source inputs in different regions (Black et al., 2020).

In this study, we use a global marine DFe data set to constrain the iron cycle fluxes in a global marine biogeochemical model. We analyze model sensitivity simulations that focus on three key uncertainties: varying source fluxes of (a) atmospheric soluble iron deposition and (b) reductive sedimentary iron release, as well as the role of a (c) variable ligand distribution on DFe distribution and scavenging rates. The resulting DFe concentrations in each model simulation are evaluated against observations to determine the most realistic marine iron cycle fluxes among the model scenarios.

2. Model Description

We used the UVic Earth System Climate Model (Weaver et al., 2001) version 2.9 (Eby et al., 2009). In the following section, we provide a general overview of the model components then focus on improvements made to the marine iron cycle in this study, whereas other modifications applied to all model simulations are described in the supplementary information.

2.1. Physical Model

The physical ocean-atmosphere-sea ice model includes a three-dimensional (1.8° × 3.6°, 19 vertical levels) general circulation model of the ocean (Modular Ocean Model 2) with parameterizations such as diffusive mixing along and across isopycnals and eddy-induced tracer advection (Gent & McWilliams, 1990). The physical configuration is based on Somes et al. (2017) and includes parameterizations such as computation of tidally induced diapycnal mixing over rough topography on the sub-grid scale (Schmittner & Egbert, 2014), anisotropic viscosity (Large et al., 2001; Somes et al., 2010), and enhanced zonal isopycnal mixing schemes in the tropics to better represent zonal equatorial undercurrents (Getzlaff & Dietze, 2013). A two-dimensional, single level energy-moisture balance atmosphere and a dynamic-thermodynamic sea ice model are used, forced with prescribed monthly climatological winds (Kalnay et al., 1996) and constant ice sheets (Peltier, 2004).

2.2. Marine Biogeochemical Model

The updated marine ecosystem-biogeochemical model coupled within the ocean circulation model is based on the Model of Ocean Biogeochemistry and Isotopes (MOBI), version 2.0. Briefly, MOBI includes three prognostic inorganic nutrient tracers (nitrate [NO_3], phosphate [PO_4], iron [DFe]) and two organic phases
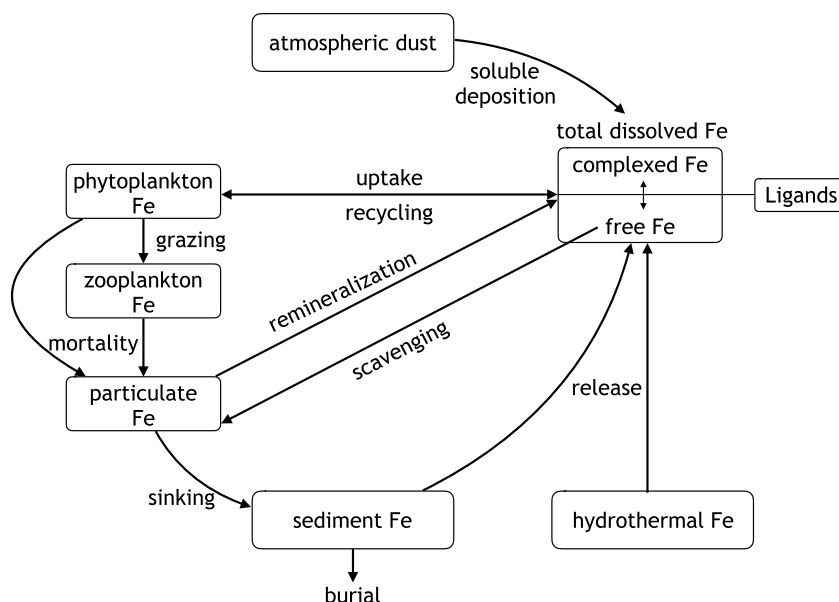
Figure 1. Schematic of the marine iron (Fe) model. See Section 2.3 for a full description.

(dissolved organic nitrogen [DON] and dissolved organic phosphorus [DOP]), three phytoplankton (ordinary, N_2-fixing diazotrophs, calcifying coccolithophores), one zooplankton, sinking detritus (i.e., dead particulate organic matter [POM]), as well as dissolved oxygen (O_2), dissolved inorganic carbon, alkalinity, and $\Delta^{14}C$ (Figure S1). It combines latest features from previous studies focusing on the nitrogen cycle (Somes & Oschlies, 2015), iron cycle (Muglia et al., 2017), and carbon chemistry (Kvale et al., 2015), and is also constrained by isotope systems of ^{13}C and ^{15}N (Schmittner & Somes, 2016) (not shown here). Our model experiments were simulated for over 5,000 years under pre-industrial boundary conditions as they approached their quasi steady state.

2.3. Marine Iron Cycle Model

2.3.1. Base Configuration

The marine iron model configuration is based on the previous UVic Kiel Marine Biogeochemistry Model (KMBM) (Nickelsen et al., 2015), including improvements implemented in Muglia et al. (2017) (Figure 1). The marine iron model includes explicit tracers for DFe and particulate iron (PFe). All phytoplankton grow with a constant elemental stoichiometry ratio of iron relative to nitrogen. The sources of DFe to the ocean are atmospheric soluble deposition (Luo et al., 2008), reductive dissolution and release from sediments (Elrod et al., 2004; Moore & Braucher, 2008), and hydrothermal fluxes (Tagliabue et al., 2010) (Table 2, Figure 2). The ligand concentration determines the fraction of DFe that is organically complexed and thus unavailable for scavenging, whereas the remaining free DFe (DFe') pool can be scavenged to PFe, which then sinks and remineralizes at the same rate as POM (Table S1). In the base simulation #1, ligands are prescribed to be globally constant at 1 nM as in previous iterations of the model. This simulation is given the name *SrcLow_LigCon* to reflect its differences (i.e., low source inputs of atmospheric soluble deposition and reductive sedimentary iron release, and constant ligand distribution) from further changes made to the marine iron model in this study (see subsections below and Tables 1 and 2).

2.3.2. Scavenging

The formulation for scavenging and partitioning of free and organically complexed DFe is based on from previous model parameterizations (Nickelsen et al., 2015; Galbraith et al., 2010). Scavenging of DFe' to PFe occurs via two mechanisms in the model: (a) absorption onto POM following (Honeyman et al., 1988; Parekh et al., 2004)

$$Fe_{OrgSc} = kFe_{org}DFe'POC^{0.58}, \tag{1}$$

Table 1
Marine Iron Model Configurations

#	Simulation name	Atmospheric soluble deposition	Reductive sedimentary release	Ligand distribution	Inorganic scavenging $(kFe_{prp}$[a]$)$	Particle scavenging $(kFe_{org}$[b]$)$
1	SrcLow_LigCon	Low[c]	Low[d]	Constant[e]	0.0069	1.2
2	SrcLow_LigVar	Low	Low	Variable[f]	0.0052	1.5
3	SedMid_LigVar	Low	Mid[g]	Variable	0.0069	2.2
4	SedHigh_LigVar	Low	High[h]	Variable	0.0081	2.9
5	Atm + SedHigh_LigVar	High[i]	High	Variable	0.0098	2.9

[a]Inorganic scavenging parameter has units of $(mmol\ Fe/m^3)^{-2}d^{-1}$. [b]Particle scavenging parameter has units of $(gC/m^3)^{-0.58}\ d^{-1}$. [c]Luo et al. (2008). [d]Elrod et al. (2004) parameterization with low flux rate (see Section 2.3.4). [e]Constant concentration of 1 nM everywhere in the ocean. [f]Variable ligand parameterization (see Section 2.3.3). [g]Dale et al. (2015) parameterization with intermediate maximum flux rate 100 μmol Fe m^{-2} d^{-1}. [h]Dale et al. (2015) parameterization with suggested maximum flux rate 170 μmol Fe m^{-2} d^{-1}. [i]Myriokefalitakis et al. (2018).

which is a function of particulate organic carbon (POC), free DFe (DFe'), and the particle scavenging rate constant (kFe$_{org}$); and (b) inorganic scavenging

$$Fe_{InSc} = kFe_{prp}DFe'^2, \qquad (2)$$

which depends only on DFe' and the inorganic scavenging rate constant (kFe$_{prp}$) following the scheme of Galbraith et al. (2010). This inorganic scavenging term primarily represents colloidal aggregation into larger, sinking particles as well as lithogenic scavenging not explicitly accounted for in our model. Here we use a non-linear formulation for inorganic scavenging following Galbraith et al. (2010) which was designed to account for high lithogenic scavenging rates to better reproduce DFe where atmospheric deposition is high (e.g., tropical and subtropical North Atlantic) (Pham & Ito, 2019; Ye & Völker, 2017). Note that we included a slightly higher non-linear exponent (2.) compared to Galbraith et al., 2010 (1.5) that better reproduced DFe in high atmospheric deposition areas in our model. This difference may be related to the fact that Galbraith et al., 2010 model included higher phytoplankton iron quotas when DFe is high which further reduces DFe in that model, whereas our model formulation assumes constant iron stoichiometry due to high uncertainties associated with this process. Thus, our model performed better with higher scavenging rates to reduce the overestimation of DFe in these high deposition areas.

In each model simulation, the scavenging rate constants (kFe$_{org}$, kFe$_{prp}$) were manually tuned so that each simulation contains a nearly identical global iron inventory with an average global DFe concentration of 0.7 ± 0.03 nM (Table 2). The inorganic scavenging rate constant was adjusted until the model reproduced the mean observed DFe concentration in the ocean interior since it is the dominant form of scavenging there, whereas the POM scavenging rate constant was adjusted to reproduce declining DFe concentrations toward the surface ocean (Figure 4). The globally integrated rates of the different scavenging processes are shown in Table 2, vertically integrated rates from high and low source input simulations in Figure 2, and total basin-scale averages in Figure 4.

2.3.3. Ligand Parameterization

In the base model configuration, a constant ligand concentration of 1 nM is applied globally, and thus has *LigCon* in its model name (see Table 1). However, the distribution of ligands in the real ocean is variable (e.g., Völker & Tagliabue, 2015). Since iron-binding ligands are thought to be produced during the production of organic matter (Gledhill & Buck, 2012), which might explain why DOM and AOU may qualitatively reflect some observed ligand concentration patterns (Misumi et al., 2013; Pham & Ito, 2018; Tagliabue & Völker, 2011). However, a first global model-data comparison with ligands simulated as prognostic tracers found ligand distributions difficult to constrain with available observations and is further complicated by large variations in binding strength of different types of ligands (Völker & Tagliabue, 2015). Therefore, to maintain computational efficiency, we pragmatically chose to implement ligand concentrations as a function of existing tracers rather than include additional prognostic tracers.

Table 2
Global Marine Iron Cycle Results

#	Simulatiosn name	Atmospheric soluble deposition (Gmol yr^{-1})	Reductive sedimentary release (Gmol yr^{-1})	Hydro-thermal (Gmol yr^{-1})	Inorganic scavenging (Gmol yr^{-1})	Particle scavenging (Gmol yr^{-1})	Dissolved iron (nM)	Global residence time[a] (yr)	Surface residence time[b] (yr)
1	SrcLow_LigCon	1.4	15.1	11.4	34.3	22.5	0.68	33.3	3.12
2	SrcLow_LigVar	1.4	14.6	11.4	30.9	29.3	0.73	35.9	2.56
3	SedMid_LigVar	1.4	68.6	11.4	99.3	55.9	0.73	12.2	1.35
4	SedHigh_LigVar	1.4	117	11.4	159	83.9	0.73	7.66	0.87
5	Atm + SedHigh_LigVar	3.4	114	11.4	162	81.5	0.71	7.49	0.83

[a]Since our iron model simulates active (re)cycling between particulates and dissolved forms and thus scavenging does not permanently remove bioavailable iron from the system, we calculate residence time based on global external fluxes and bulk inventory, that is, global Fe inventory/∑Source Inputs. [b]For surface residence time, we follow Black et al. (2020) by including the upper 250 m and account for sinking particulate iron out of this layer as the sink flux. Since our particulate iron pool includes both biogenic (i.e., produced during primary production) and authigenic (i.e., produced by scavenging) iron in the model, this model residence time is comparable to their mean dissolved, biogenic + authigenic estimate, which ranges from 0.1 to 4 years depending on location.

We implemented a variable ligand parameterization to estimate ligand concentrations based on a function of DON and AOU:

$$Lig = \alpha AOU^{0.8} + \beta DON^{0.8}, \tag{3}$$

where α (0.015 nmol ligand/(mmol O_2 m^{-3})$^{0.8}$) and β (0.21 nmol ligand/(mmol DON m^{-3})$^{0.8}$) are generic parameters that determine ligand concentration associated with the tracers AOU and DON, respectively. The parameters α and β were chosen so that the global ligand mean concentration remained at 1 nM, consistent with simulation #1 with constant ligands, but now reflects changes in their spatial distribution (Figure 3). Model simulations with this variable ligand parameterization (simulations #2–5, see Table 1) have *LigVar* in their respective model simulation name.

Although we follow previous studies for the variable ligand parameterization (Misumi et al., 2013; Pham & Ito, 2018; Tagliabue & Völker, 2011), a few notable changes have been made in our version. Since AOU can be negative in the surface ocean due to dissolved oxygen supersaturation, we applied a minimum ligand concentration of 0.5 nM. Previous ligand parameterizations have also applied minimum ligand concentrations to account for ligands associated with more refractory forms of DOM not explicitly included in our model (Aumont et al., 2015; Tagliabue & Völker, 2011). We also applied an exponential parameter (0.8) to the AOU and DON terms, which reduces ligands associated to these tracers particularly when their concentrations are high. This helped the model from overestimating DFe concentrations when AOU and DON concentrations are at their highest concentrations in the model.

2.3.4. Reductive Sedimentary Iron Release Parameterization

The base model version uses reductive sedimentary iron release based on the Moore and Braucher (2008) implementation of Elrod et al. (2004),

$$Fe_{sed} = \gamma_{FeSed} C_{ox}, \tag{4}$$

where the Fe flux from the sediments (Fe_{sed}) is determined by the sedimentary iron release rate (γ_{FeSed} = 0.27 μmol Fe/mmol C_{ox} m^{-2} d^{-1}), and organic carbon oxidation (C_{ox}) in the sediments. The base model version uses the DFe flux rate from Nickelsen et al. (2015) that is lower than suggested by Elrod et al. (2004) (0.72 μmol Fe mmol C_{ox}^{-1} m^{-2} d^{-1}). Since this formulation yields lower global rates of this source input in the model compared with other implemented sedimentary functions included in this study (described below), model simulations with this sedimentary iron release implementation (#1–2) contain the name *SrcLow*, noting they also include a low source input of atmospheric soluble iron deposition (see Section 2.3.5 below).

We also implemented the sedimentary iron release function proposed by Dale et al. (2015), who compiled a global data set of sedimentary DFe fluxes to constrain their model estimate. While it has a strong depend-
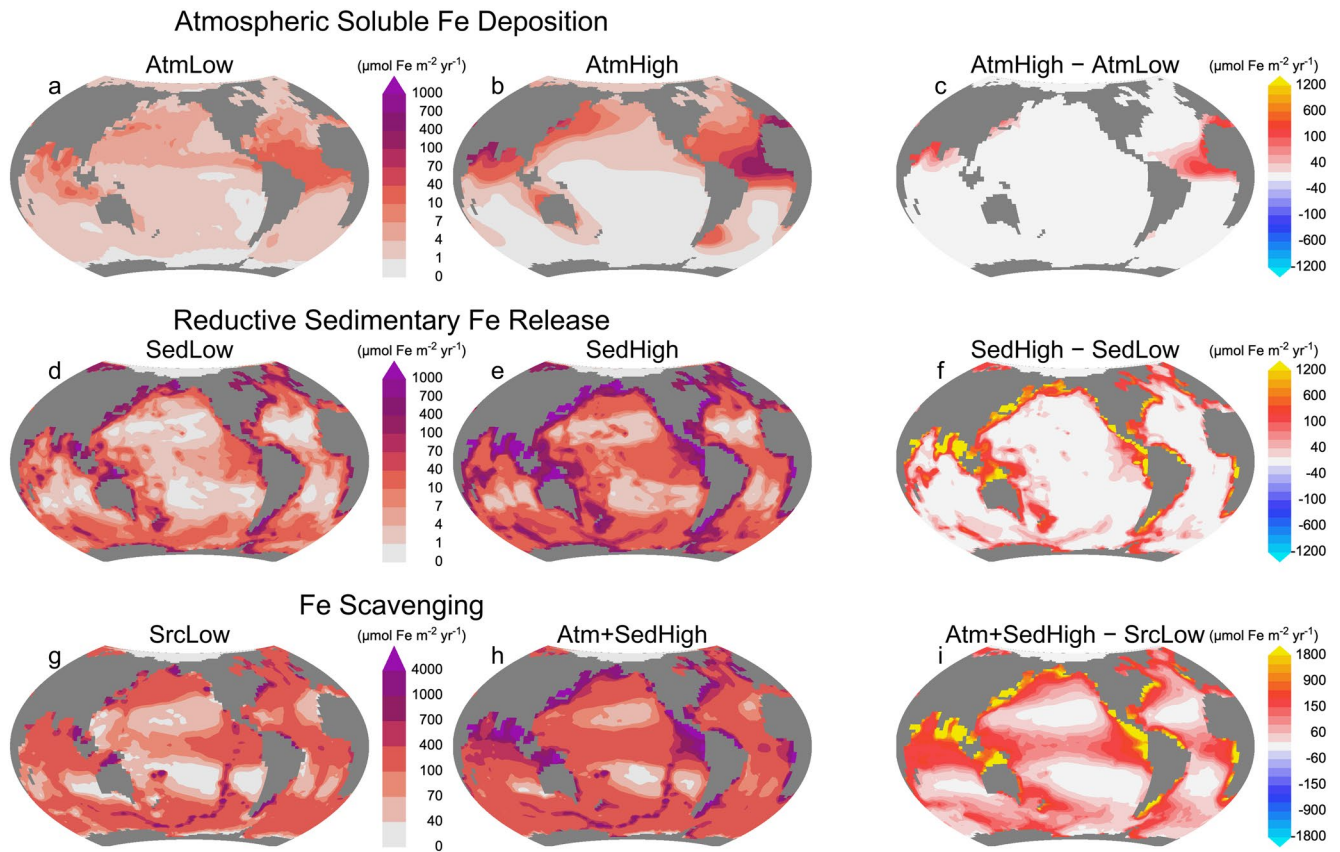
Atmospheric Soluble Fe Deposition

Figure 2. Vertically integrated fluxes of atmospheric soluble iron deposition (top row) prescribed on model simulations #1–4 from Luo et al. (2008) (*AtmLow*) (a), high scenario (*AtmHigh*) from the GESAMP intermodel average (Myriokefalitakis et al., 2018) (b), and their difference (c). Center row: Vertically integrated sedimentary iron release using parameterizations based on Elrod et al. (2004) (*SedLow* from simulation #2) (d) and Dale et al. (2015) (*SedHigh* from simulation #4) (e), and their difference (f). Bottom row: Vertically integrated total scavenging rates from simulation #2 with low source inputs and scavenging rates (*SrcLow*) (g) and simulation #5 with highest rates (*Atm + SedHigh*) (h), and their difference (i).

ence on the flux of POM to the seafloor similar to Elrod et al. (2004), the data set in Dale et al. (2015) also revealed a strong dependence on bottom water oxygen concentration. Dale et al. (2015) thus parameterized sedimentary DFe release as

$$Fe_{sed} = \gamma_{FeSedMax} tanh\left(C_{ox} : bwO_2\right),$$ (5)

where $\gamma_{FeSedMax}$ is the maximum flux under steady-state conditions, and bwO_2 is dissolved oxygen concentration in bottom waters interacting with the sediments.

We test two scenarios with the Dale et al. (2015) parameterization by altering the maximum flux constant ($\gamma_{FeSedMax}$). The *SedHigh* simulations apply the value suggested by Dale et al. (2015) ($\gamma_{FeSedMax} = 170$ μmol m^{-2} d^{-1}), whereas the *SedMid* simulation reduces the maximum flux value to 100 μmol m^{-2} d^{-1} to test more a intermediate level of sedimentary DFe release (see Tables 1 and 2). This reduced value was chosen to test a global sedimentary DFe flux approximately halfway in between *SedHigh* and *SedLow* since their fluxes differ by a large amount. Note that the *SedMid* simulation does not produce a significantly different spatial distribution compared to *SedHigh*.

2.3.5. Atmospheric Soluble Iron Deposition

We applied the atmospheric soluble iron deposition mask from Luo et al. (2008) in model simulations #1–4. This atmospheric soluble iron deposition estimate delivers 1.4 Gmol yr^{-1} of soluble iron to the global ocean, which is on the low-end (AtmLow; see Figure 2) compared to other estimates applied in the marine iron model intercomparison study (Tagliabue et al., 2016). This estimate from Luo et al. (2008) is one of the first

Variable Ligand Distribution

Surface (0-250m)

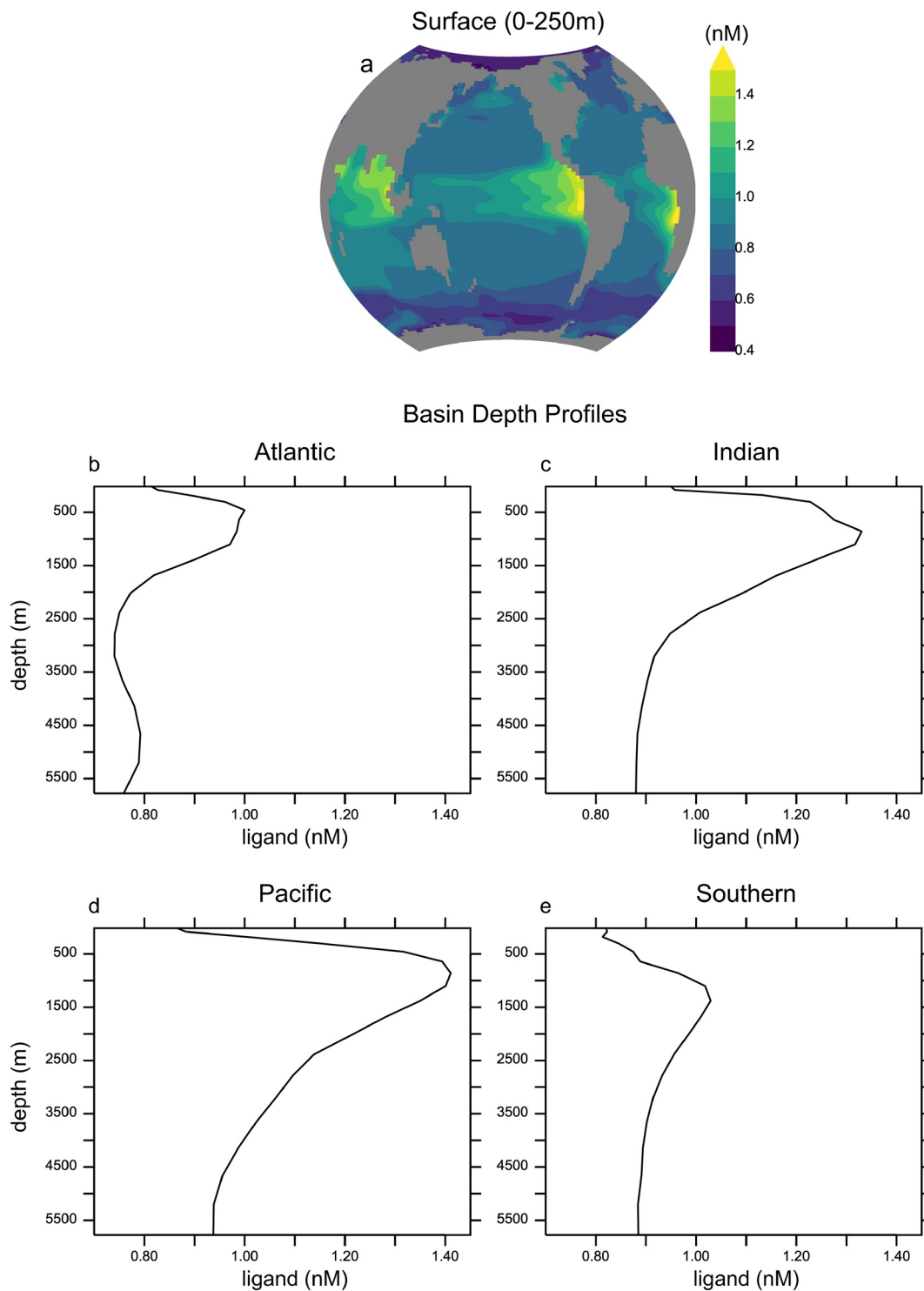

Basin Depth Profiles

Figure 3. Distribution of variable ligand concentrations in the surface (0–250 m) ocean (a), and basin-scale averages in the Atlantic (b), Indian (c), Pacific (d), and Southern (e). Note that the Southern Ocean region (>40°S) from within the other basins (b)–(d) is excluded there since it is shown in (e).
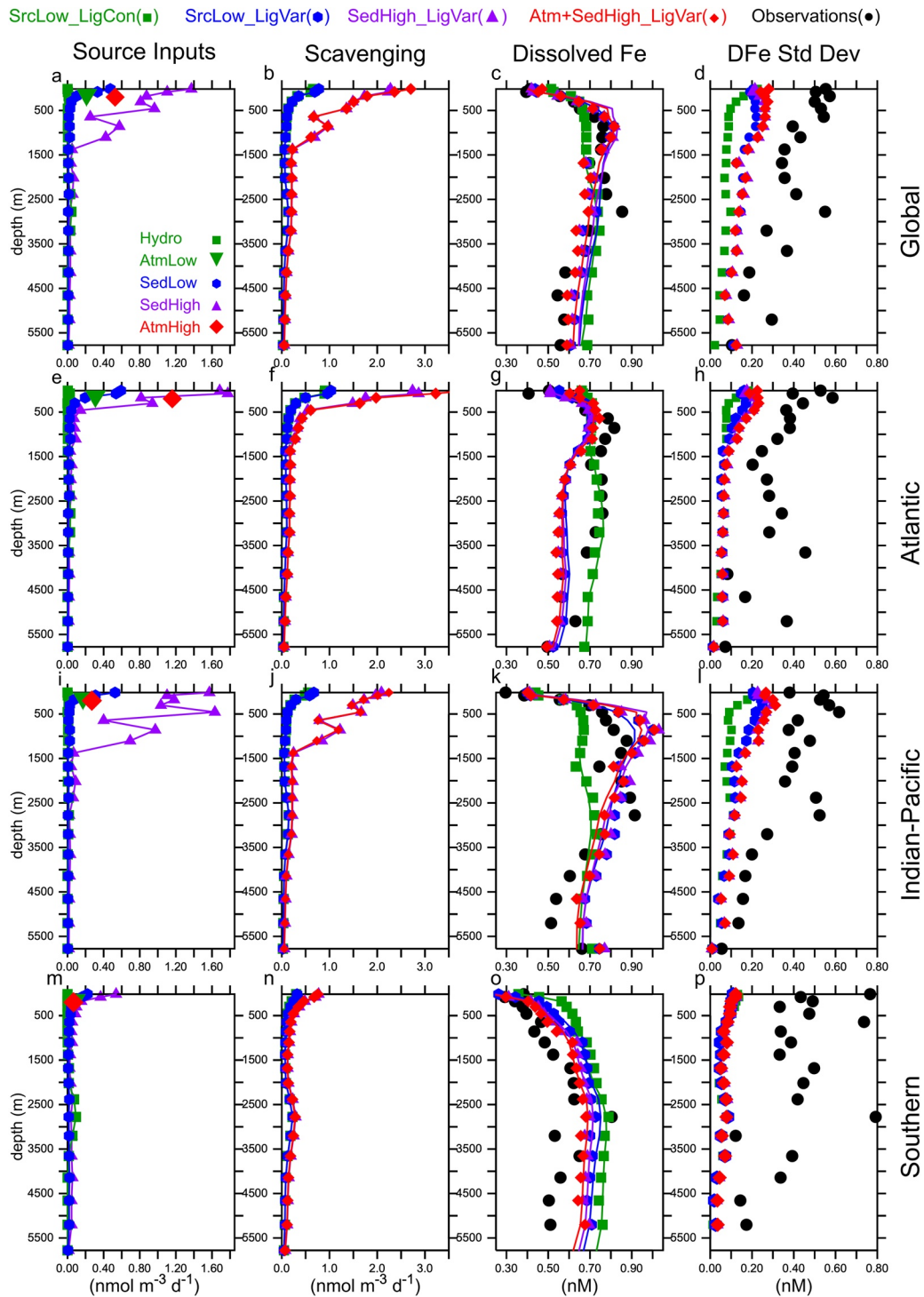
Figure 4. Annually averaged depth profiles of marine iron source inputs (left column), scavenging rates (center-left column), dissolved iron concentrations (center-right column), and dissolved iron (DFe) standard deviation (Std Dev) (right column) in the Global, Atlantic, Indian-Pacific, and Southern Ocean for model simulations (colored symbols) and dissolved iron observations (black circles). Source inputs (left column) are atmospheric soluble deposition as large filled symbols in the low scenario (AtmLow, green down-pointing triangle) and high (AtmHigh; red diamonds) scenarios, sedimentary iron release in the low (SedLow; blue hexagons) and high scenarios (SedHigh; purple triangles), and hydrothermal flux (green square, applied to all simulations). For dissolved iron concentrations (center-right column), lines show model averages in the entire selected domain, while symbols include model results only where dissolved iron observations exist. Note that the Southern Ocean region (>40°S) from within the Atlantic and Indian-Pacific basins is excluded there since it is shown in the Southern Ocean panels.

deposition models that explicitly accounted for the soluble iron deposition rather than assuming a constant solubility from total deposition.

Another estimate we test in this study applies the average flux from four recent atmospheric soluble iron deposition models (Myriokefalitakis et al., 2018). The intermodel average global soluble deposition rate is 3.4 Gmol yr^{-1} with similar patterns to Luo et al. (2008) but higher rates most notably in the North Atlantic. This simulation with high atmospheric soluble iron deposition (AtmHigh; Figure 2) is applied to the simulation with high sedimentary release and variable ligands and is therefore named *Atm + SedHigh_LigVar*.

3. Model Results and Data Comparison

3.1. Global Dissolved Iron Data Set

The DFe database used in this study is a collection of observations from both GEOTRACES Intermediate Data Product 2017 (7,520 points; Schlitzer et al., 2018) and prior observations compiled by Tagliabue et al. (2012) (12,371 points). Note that we excluded 37 measurements (19 from GEOTRACES, 18 from prior) with high DFe concentrations between 10 and 216 nM mainly from locations with high hydrothermal activities, but also some near-shore settings (e.g., Laptev Sea, Bristol Bay, Peruvian coastal waters near urban area of Trujillo) and around small islands not resolved in the model (e.g., Kerguelen, Indonesian and Coronation), and thus the data set used here contains concentrations up to 10 nM. We then interpolated the data onto the UVic model grid using the PyFerret SCAT2GRIDGAUSS function developed by NOAA's Pacific Marine Environmental Laboratory, which is a Gaussian interpolation function based on Kessler and McCreary (1993). This gridded data was used for the model-data comparison (Figures 3–7) and to calculate model-data statistical metrics (i.e., correlation coefficient, (uncorrected) standard deviation, and root-mean-squared error) (Figure 8). It covers 5,917 grid points since many observations overlap and thus are averaged on corresponding grid points. Since we compare to annual model results, we interpolated all observations onto the grid and thus temporal aspects and variability of the data are not taken into account or investigated in this study.

Model-data misfit statistical metrics are sensitive to unresolved outlier concentrations and spatial extent of the data interpolation onto the model grid. However, these aspects do not affect which simulations best reproduce the global data set according to statistical metrics. This is illustrated by comparing metrics calculated from all observations (triangles) to only GEOTRACES (circles) in Figure 8. The statistical metrics slightly improve when comparing against only GEOTRACES observations, with the only exception being root-mean-squared error for model simulation #1 in the surface ocean, but the relative improvements in the model simulations are nearly identical. The arbitrary exclusion concentration threshold of 10 nM was chosen as a balance between including as many observations as possible while still being able to calculate useful statistical metrics that are not dominated by these outlier concentrations.

3.2. Variable Ligand Distribution

The simulation with constant ligands does not reproduce the major basin-scale features of the observed DFe distribution, despite that its globally averaged depth profile is generally consistent with observations (Figure 4c). Most notably, simulations with constant ligands significantly overestimate the DFe in the interior Southern Ocean (Figure 4o), a critical ocean basin for Fe-limited phytoplankton growth. *LigCon* thus overestimates supply of DFe via upwelling, and underestimates Fe limitation of phytoplankton growth, which is a key deficiency in the base configuration and previous model versions (e.g., Muglia et al. (2017)). They also underestimate DFe in intermediate waters in the Indian and Pacific Ocean (Figures 4k and 5b), which we have averaged together since they have similar deep ocean biogeochemical tracer profiles relative to the global average (Figure S1).

The simulations with variable ligand concentrations (#2–5; *LigVar*) better reproduce the ocean interior distribution of DFe (Figure 5). This is primarily due to the AOU dependence of the variable ligand parameterization that mainly determines ligand concentrations in the deep ocean since semi-refractory DOM concentrations are low there in the model. This is most obvious when comparing intermediate depths of the
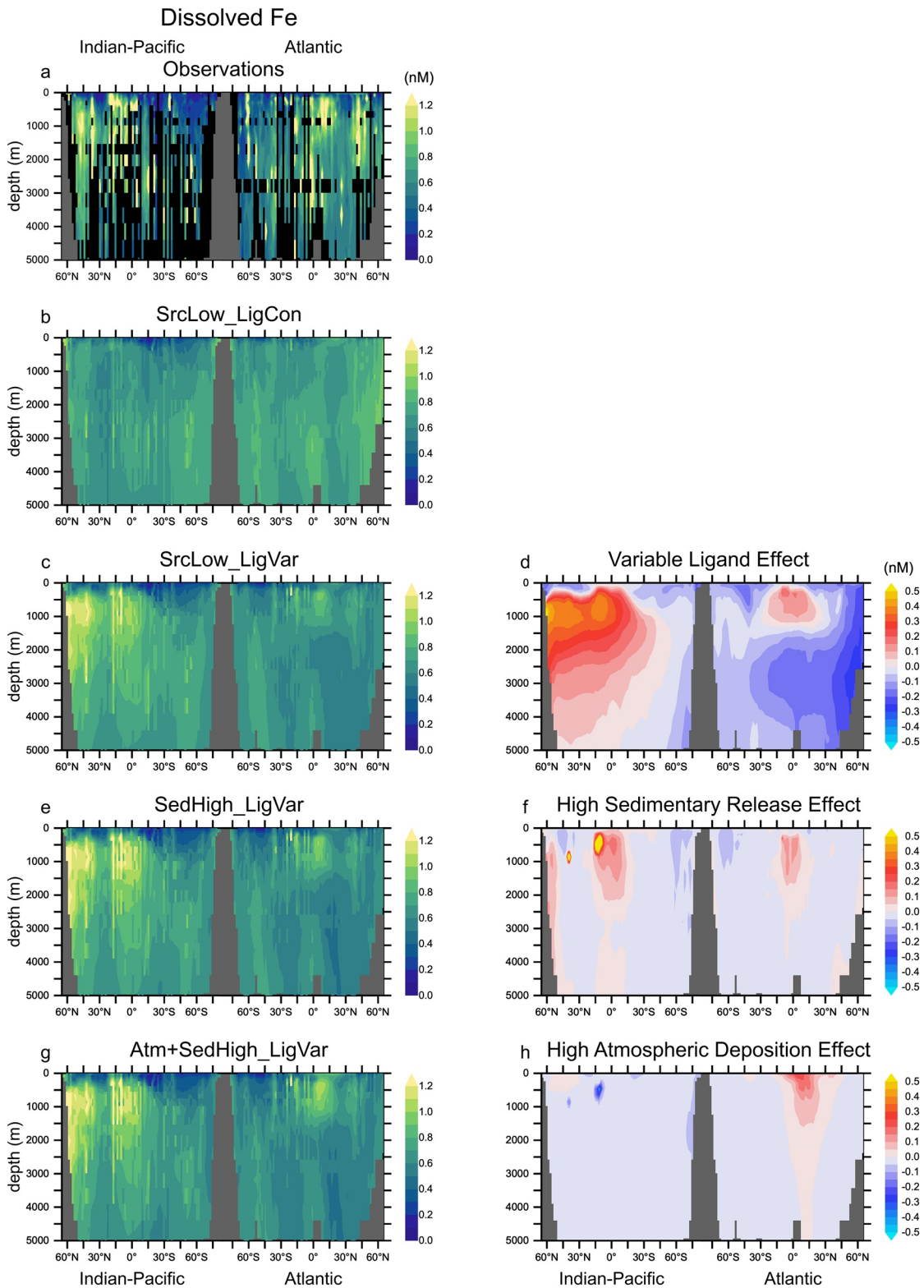
Figure 5. Annual, zonally averaged dissolved iron concentrations in the Indian-Pacific and Atlantic basins in observations (a), *SrcLow_LigCon* (b), *SrcLow_LigVar* (c), *SedHigh_LigVar* (e), and *Atm + SedHigh_LigVar* (g). Right column highlights individual effects on dissolved iron concentrations by showing model differences from variable ligands (i.e., *SrcLow_LigVar − SrcLow_LigCon*) (d), high sedimentary iron release (i.e., *SedHigh_LigVar − SrcLow_LigVar*) (f), and high atmospheric soluble deposition (i.e., *Atm + SedHigh_LigVar − SedHigh_LigVar*) (h). In locations where no observations exist (black region in a), zonal model averages are shown (b,c,e,g).
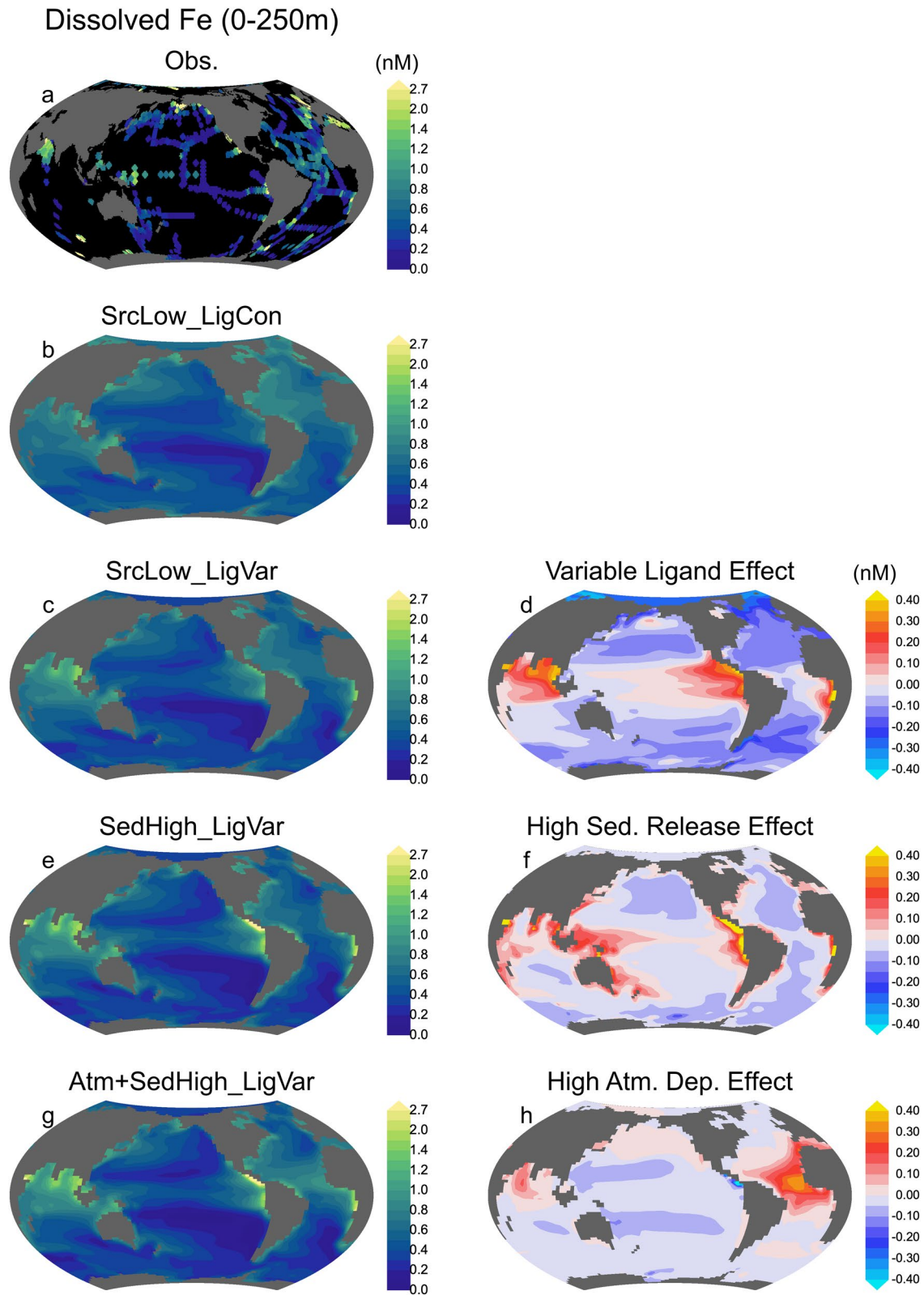
Figure 6. Annually averaged dissolved iron concentrations in the upper 250 m in observations (a), *SrcLow_LigCon* (b), *SrcLow_LigVar* (c), *SedHigh_LigVar* (e), and *Atm + SedHigh_LigVar* (g). Right column highlights individual effects on dissolved iron concentrations by showing model differences from variable ligands (i.e., *SrcLow_LigVar − SrcLow_LigCon*) (d), high sedimentary iron release (i.e., *SedHigh_LigVar − SrcLow_LigVar*) (f), and high atmospheric soluble deposition (i.e., *Atm + SedHigh_LigVar − SedHigh_LigVar*) (h).
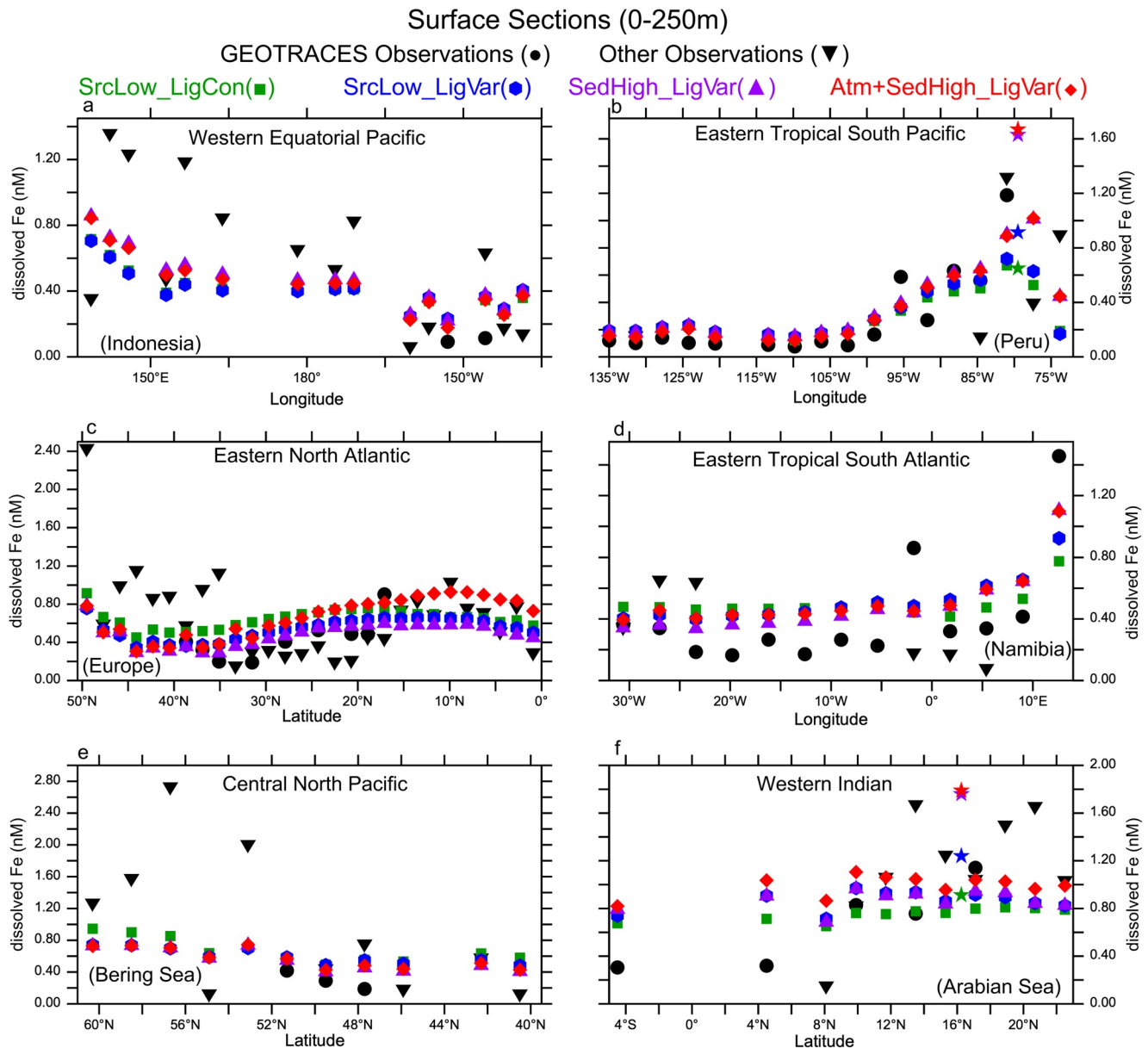
Figure 7. Comparison of dissolved iron measurements from GEOTRACES (black circles) and others (black down-pointing triangles) in the upper 250 m with model simulations *SrcLow_LigCon* (green squares), *SrcLow_LigVar* (blue hexagons), *SedHigh_LigVar* (purple triangles), *Atm + SedHigh_LigVar* (red diamonds) across ocean the western equatorial Pacific (10°S–10°N) (a); eastern tropical South Pacific (5°S–15°S) (b); eastern North Atlantic (30°W–0°) (c); eastern tropical South Atlantic (35°W–15°) (d); central North Pacific (175°–150°W); and western Indian (zonal averaged from 20° to 100°E) (c). The intersecting continental margin or shelf sea at the end of the transect is given in parenthesis. Model results are included only at locations where observations exist. Since the core of oxygen deficient zones in the model does not directly overlap with the real ocean where high dissolved iron concentrations exist in the eastern tropical South Pacific (b) and northern Indian Ocean (f), we added dissolved iron concentrations directly above the core of the oxygen deficient zones ($O_2 < 5$ mmol m^{-3}) in the model as star symbols.

Southern and Indian-Pacific Oceans, which contain relatively low and high values of AOU and thus ligand concentrations, respectively, according to our parameterization (see Figures 3 and S1). Lower ligand concentrations in the Southern Ocean enhances scavenging causing lower DFe concentrations, with the opposite effect occurring in the Indian-Pacific Ocean, resulting in better reproduced observations in both basins. Therefore, the interior DFe distribution with the variable ligand parameterization is better partitioned with respect to observations (Figures 4 and 5) and improves the global model-data misfit by 9.2% when averaging across our three metrics (i.e., correlation coefficient (R), normalized standard deviation (nSTD), and
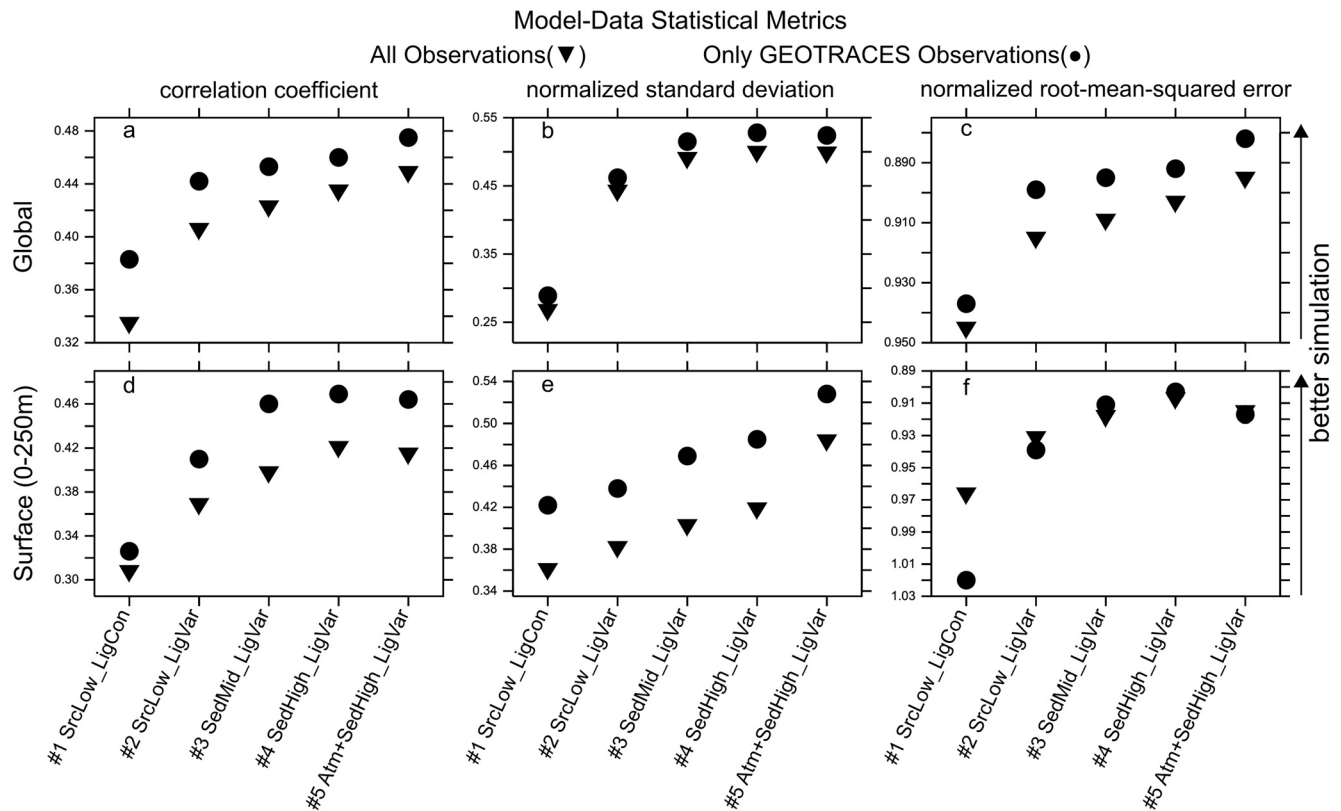
Figure 8. Model-data statistical misfit metrics calculated using all observations (triangles) and using only GEOTRACES observations (circles). Correlation coefficient (left column), standard deviation (center column), root-mean-squared error (right column) are calculated for the global ocean (top rows) and upper 250 m of the water column (bottom rows). Standard deviation (b, e) and root-mean-squared error (c, f) are normalized by the standard deviation of observations. The root-mean-squared error vertical axis has been inverted so the upwards direction represents a better model misfit in all panels. Note a perfect representation of observations would yield the value 1 for correlation coefficient, 1 for normalized standard deviation, and 0 for normalized root-mean-squared error.

normalized root-mean-squared error (nRMS); ($\Delta R + \Delta nSTD + \Delta nRMS \cdot -1$)/3 × 100%) against all observations (Figure 8), which represents the largest improvement from any individual simulation in this study.

The concentration of semi-refractory DON largely determines ligand concentrations in the surface ocean (Figure 3a). DON concentrations are higher around the high productivity regimes in the low latitudes with generally decreasing values toward higher latitudes (Somes & Oschlies, 2015) (Figure S2). This pattern is reflected in the surface DFe distribution that shows the same latitudinal trend in the variable ligand model (Figures 6c–6d). While this meridional DFe pattern better reproduces low DFe concentrations in the open Southern Ocean, it creates larger model-data biases on high latitude continental shelves in the Bering Sea, Weddell Sea, and European shelf seas (Figures 6a–6d, 7c and 7e). This shows that while the overall variable ligand effect significantly improves the global DFe distribution (Figure 7), model-data biases in some regions (e.g., high latitude continental shelf seas) still increase, which contributes to a smaller average metric improvement (3.9%) in the surface layer compared to the global ocean.

3.3. Sedimentary Iron Release

The simulations with low sedimentary source inputs (#1–2 SrcLow) provide a relatively poor fit to observed DFe concentrations according to the statistical metrics (Figure 8). They fail to reproduce the high DFe concentrations near continental margins (Figures 6 and 7), suggesting higher sedimentary release rates are necessary to explain these features. The simulated DFe distribution also lacks the strong spatial gradient toward depleted concentrations in many open ocean regions in the observations. These overly smooth gradients in

SrcLow are the result of low sedimentary release rates and subsequent low scavenging rates that are then required to reproduce the global mean DFe inventory, resulting in a relatively long global mean residence time of 35 years among our simulations (Table 2).

The simulations with higher sedimentary release rates (Figure 2e) produce higher DFe concentrations in continental shelf seas (Figures 6 and 7), particularly where bottom water oxygen is low in the low latitudes. The simulations applying high-end sedimentary Fe release rates (*SedHigh*) modestly outperformed simulations assuming lower rates across all calculated statistical metrics (Figure 8) on average by 3.3% in the global ocean and slightly higher by 3.8% in the surface layer, with the intermediate release rate scenario *SedMid* performed between *SedLow* and *SedHigh*. Therefore, our model-data analysis suggests that high-end estimates for global reductive sedimentary iron release rates are the most realistic.

One region that was notably improved by high sedimentary release rates was the low latitude margins near oxygen deficient zones (ODZs) (Figures 6 and 7). Observations there in both the eastern tropical South Pacific off Peru (Figure 7a), eastern tropical South Atlantic off Namibia (Figure 7d), and northern Indian Ocean show high DFe concentrations that are best reproduced in *SedHigh* scenarios. Since *SedHigh* simulations also contain high scavenging rates, they better reproduce the lowest DFe concentrations in the offshore open ocean locations as well.

The high DFe concentrations on high latitude continental shelf systems (Figures 6, 7c and 7e) are not improved in *SedHigh_LigVar* due to the interactions with ligands and scavenging. Decreasing surface ligand concentrations toward high latitude systems (Figure 3) allow scavenging to compensate the additional sediment-derived DFe more efficiently, in contrast to low latitude systems near ODZs (e.g., Tropical Pacific) that contain higher ligands allowing DFe to be retained in the water column. This causes the simulation with constant ligands to retain slightly higher DFe compared to simulations with variable ligands in high latitude continental shelf systems (e.g., Bering Sea (Figure 7c) and European Shelf Seas (Figure 7e)), despite that these simulations with variable ligands include much higher sedimentary release rates there (e.g., *SedHigh_LigVar*, Figure 2). This demonstrates that more efficient scavenging rates associated with low ligands can overcompensate the high sedimentary release rates in determining DFe concentrations in the model.

3.4. Atmospheric Soluble Deposition

The two soluble atmospheric deposition scenarios tested here predict similar spatial depositional patterns (Figure 2), with the more recent GESAMP intermodel average (Myriokefalitakis et al., 2018) providing a significantly higher global deposition rate (3.4 Gmol yr^{-1}) relative to the low estimate from Luo et al. (2008) (1.4 Gmol yr^{-1}). These enhanced rates cause higher DFe concentrations mainly from the Saharan dust plume in subtropical North Atlantic, but also to a lesser degree in the Arabian Sea and North Pacific (Figures 6g, 6h, 7c and 7f). The impact of including higher soluble deposition only slightly improves the global model-data statistical metrics by 0.7% globally and 1.5% in the surface layer, making it difficult to determine the most realistic rates based on our model-data DFe comparison alone.

3.5. High Scavenging Effect

In model simulations with high source fluxes (e.g., #5 *Atm + SedHigh_LigVar*), higher scavenging rates are necessary to maintain a realistic global DFe inventory (Tables 1 and 2, Figures 2h–2i and 3). Scavenging is thus more efficient at reducing DFe concentrations in the high source flux simulations. In regions far away from the source fluxes, particularly in the deep ocean and open Southern Ocean (e.g., see Figure 6), the model simulations with higher source fluxes actually contain lower DFe because the enhanced scavenging outweighs the source fluxes in these areas (Figure 4). Lower DFe concentrations in these deep and open ocean regions better reproduce observations further improving the model-data misfit metrics (Figure 8). The combined effects of high atmospheric and sedimentary source inputs, which also includes highest scavenging rates, contributed to the largest improvement in the surface ocean across our metrics (5.5% improvement relative to *SrcLow_LigVar*).

4. Discussion

4.1. Model-Data Constraints and Uncertainties

The variable ligand parameterization improved the model's ability to reproduce the global distribution of DFe observations the most. This is most evident in the interior ocean due to AOU dependency of this parameterization. Since ligands are produced when dissolved oxygen is consumed during the respiration of POM via heterotrophic microbes in the variable ligand parameterization, their concentrations reach maximum values in old Pacific intermediate waters (Figure 3). High ligands reduce scavenging that causes the model to better reproduce high observed DFe concentrations there (Figures 4k and 5c), a feature that has also been demonstrated in other models (Misumi et al., 2013; Pham & Ito, 2018; Frants et al., 2016). This model improvement suggests that ligand production by heterotrophic bacteria is a key mechanism maintaining the global marine iron cycle.

The model simulations that include higher source inputs and scavenging rates show a subtle but continuous improvement in the model-data misfit metrics particularly in the surface ocean (Figure 8). This is in contrast to the intermodel comparison study of Tagliabue et al. (2016), which showed no clear relationship between model performance and source inputs, as well as an inverse modeling study of Pasquier and Holzer (2017), which could not find an optimal solution among their large set of model simulations varying source inputs. However, Pasquier and Holzer (2017) only tested relatively low sedimentary release rates (up to 22 Gmol/yr compared to 117 Gmol/yr in this study) and also did not include an oxygen dependency that has a strong influence in our parameterization. Our analysis emphasizes that future modeling studies should test these important factors associated with reductive sedimentary DFe release that contributed to the model improvements in this study.

The ligand and high sedimentary DFe release effects have similar impacts on DFe spatial distributions making it difficult to constrain their individual impacts with DFe concentrations alone. This spatial overlap is most pronounced above ODZs in the eastern tropical Pacific, eastern tropical Atlantic, and Northern Indian Ocean (Figure 6). This spatial covariance occurs because when AOU is high, bottom water oxygen is typically low. Therefore, DFe concentrations are enhanced both by reduced scavenging due to high ligands where AOU is high, as well as by higher sedimentary DFe release rates where bottom water oxygen is low. Future studies should examine the integrative DFe cycling in these systems (e.g., sedimentary release and scavenging rates, ligand concentrations) to give additional insights on individual processes contributions to total DFe concentrations.

Despite high sedimentary release rates, the *SedHigh* model simulations still underestimate DFe on most continental shelf systems (Figure 7). The poorly resolved coastal dynamics in our coarse resolution circulation model is likely a key model deficiency preventing the model from representing many coastal dynamics where sedimentary DFe fluxes are high. Coarse resolution models underestimate coastal upwelling and the nutrient input on narrow shelf systems that drive productivity. This bias causes underestimated POM production as well as overestimated dissolved bottom water oxygen concentrations, both of which contribute to underestimating reductive sedimentary DFe release rates on coastal shelf systems.

Further complicating matters are interactions between sedimentary DFe release rates, ligands, and scavenging. For example, our *SedHigh_LigVar* model simulation releases significantly higher DFe on high latitude shelves (Figures 2e–2f). However, only a small part of this DFe remains in the dissolved pool since scavenging efficiently converts it to particulate iron that eventually sinks back to the sediments (Figures 2h–2i). Therefore, our model underestimation of DFe concentrations remains despite high DFe release rates. This strong spatial coupling between source and scavenging fluxes has also been demonstrated in other modeling studies (Frants et al., 2016; Pasquier & Holzer, 2017), which also found that this tight spatial coupling significantly contributes to the difficulty in constraining source inputs. The exclusion of riverine inputs that may also directly include ligands could also contribute to overly efficient scavenging resulting in underestimated DFe. If our ligand parameterization predicted higher concentrations on these high latitude shelf systems, which has been indicated by ligand observations (Völker & Tagliabue, 2015), this would prevent rapid scavenging of DFe released from sediments and better reproduce observations.

Sedimentary DFe release rates may still be underestimated even in our high release scenario. Note that our highest tested global sedimentary release rate (117 Gmol yr^{-1}) was not the highest from the marine iron model intercomparison (up to 194 Gmol yr^{-1}) (Tagliabue et al., 2016), and every model scenario tested here with increased source fluxes improved the model-data misfit metrics (Figure 8). Potentially important sedimentary processes not included in the model are non-reductive dissolution and release from reactive sediments in tectonically active or volcanic regions (Conway & John, 2014; Homoky et al., 2013) and sedimentary colloidal production (Homoky et al., 2021), which could further contribute to higher total sedimentary DFe release rates that may improve the model-data misfit.

An important limitation of applying these empirical functions of reductive sedimentary DFe release (e.g., Dale et al., 2015; Elrod et al., 2004) in global models is that total iron balance within the sediments is not explicitly accounted for. Thus, these parameterizations can potentially represent an unlimited long-term supply of DFe to the ocean which is unrealistic. This simplification can be justified because many important sources of particulate Fe to the sediment are not yet included in the model, for example, atmospheric and riverine input of lithogenic material and in situ production at volcanic islands or active margins, which provide DFe for release. Also note that the Dale et al. (2015) parameterization applied in the *SedHigh* simulations sets a maximum rate determined under steady-state conditions which caps potentially unrealistic high release rates. While this simplification is likely not a significant deficiency in steady-state model simulations presented here, this should be considered in transient simulations with substantial enhancement of sedimentary DFe fluxes.

Atmospheric deposition often occurs at high rates over continental shelves (e.g., North Pacific, Patagonia) and ODZs (e.g., Arabian Sea), again making it difficult to constrain individual processes driving DFe concentrations when multiple processes act together in close spatial proximity. For example, our high atmospheric soluble deposition scenario helps reproduce high DFe concentrations in the Arabian Sea (Figure 7f). However, our model underestimates the extent of the Arabian Sea ODZ which could be the real cause driving high DFe concentrations there via high sedimentary DFe release, reduced scavenging, and/or enhanced redox cycling (Moffett et al., 2007). Instead the model ODZ is mostly misplaced to the Bay of Bengal, where higher simulated DFe there in the model better matches observations within the real ODZ in the Arabian Sea (see star symbols in Figure 7f).

The model simulations do not resolve the high variance of the observations which is reflected in the underestimated standard deviation (Figures 4 and 8). This occurs everywhere in the ocean and is most pronounced in the Southern Ocean due to it containing very low DFe in the open ocean but also high concentrations near islands, continental margins, and hydrothermal vents (Figures 4–6). Although not a focus of this study, the model was not able to reproduce the full spatial extent of high DFe concentrations near hydrothermal vents at mid-ocean depths (Figures 4 and 5), despite that this source is included (Table 2). Previous modeling studies were only able to reproduce this high DFe extent when assuming that the hydrothermal vents were also a significant source of ligands (Frants et al., 2016; Resing et al., 2015) or included stabilization via reversible scavenging (Roshan et al., 2020), both of which we have not accounted for in our model. This emphasizes that future model versions should include all important ligands and scavenging dynamics to better represent their importance in marine iron models, but that a more robust global database of ligand concentrations including their binding strength would be required (Völker & Tagliabue, 2015).

High variance in the global data set may not reflect mean climatological conditions simulated by the preindustrial steady-state model results given the highly dynamic nature of DFe cycling particularly in the surface ocean with short residence times (Black et al., 2020). The spatial and temporal sparsity of the data set likely contribute to high variance as well. But note that the standard deviation was significantly improved in our best model simulation with variable ligands and high source/scavenging fluxes (*Atm + SedHigh_LigVar*; see Figures 4, 8b and 8e) suggesting that a model with low residence times can better reproduce the high variance and strong gradients in the DFe observations. Since most DFe observations have been collected in recent decades, there could already be a significant anthropogenic impact (e.g., enhanced deoxygenation, atmospheric/riverine pollutants) on the global marine iron cycle not included in these model simulations, especially if the marine DFe residence time operates on decadal timescales or less. Future additions and expansion to the global DFe data set as well as comparison with transient model simulations at the same period of data collection will improve uncertainties in future model-data analyses.

Table 3
Global Marine Biogeochemistry Results

#	Simulation name	Net primary production (Gt C yr^{-1})		Export production (Gt C yr^{-1})		Dissolved O$_2$ (mmol m^{-3})	
		Global	Southern	Global	Southern	Global	Southern
1	SrcLow_LigCon	47.0	8.11	8.1	2.12	167	206
2	SrcLow_LigVar	47.4	7.09	7.9	1.86	175	216
3	SedMid_LigVar	47.7	6.72	7.9	1.75	178	221
4	SedHigh_LigVar	48.0	6.67	7.9	1.74	179	222
5	Atm + SedHigh_LigVar	47.9	6.42	7.8	1.68	181	224

4.2. A Global Marine Iron Cycle With a Residence Time Under a Decade?

Our model simulations testing various external source fluxes in the global marine iron cycle result in global average residence times ranging from 7.5 to 36 years. The simulation that best reproduces the observations (*Atm + SedHigh_LigVar*) has the lowest residence time (global: 7.5 years; surface ocean: 0.83 years) among our model experiments. This low-end residence time is caused in large part due to the high source fluxes, with the reductive sedimentary release being the most important with the highest global rate in our simulations. These high source fluxes need to be compensated by efficient scavenging and subsequent removal via burial in the sediments to reproduce the distribution and global mean inventory in DFe observations, a model feature that was also found in other modeling studies (e.g., see Frants et al., 2016; Pasquier & Holzer, 2017).

This is in general agreement with observational studies focusing on the surface layer (Black et al., 2020; Sarthou et al., 2003). For example, Black et al. (2020) estimated similar residence times throughout the global surface ocean (0–250 m) for DFe ranging from approximately 1 month to 4 years depending on the region and specific iron pools considered, although noting that the uncertainties remain large (i.e., equal or greater than the absolute value of the estimate in each region). These generally low surface residence times are captured in our model simulations that range from 0.83 to 3.12 years (Table 2). However, residence times of individual molecules and regions can further vary depending on the local coupling of source inputs, scavenging efficiency, and regeneration (e.g., Holzer et al. (2016); Pasquier and Holzer (2018); Tagliabue et al., 2019). For instance, DFe in the ocean interior is more stable and controlled by the amount of ligands that reduces scavenging and removal to the sediments via sinking particulates, contributing to the longer global residence times.

4.3. Marine Iron Flux Impacts on Global Ocean Biogeochemistry

An interesting feature of the model simulations is that there is surprisingly little change to globally averaged marine productivity and export production (Table 3). This occurs in large part in the model because scavenging was also increased in high sedimentary iron release scenarios, and thus much of the additional DFe fluxes from the sediments is efficiently scavenged to particulate iron that sinks back to the sediments before it can be transported to the surface ocean where it may stimulate additional productivity. This general impact was also found in a model study using a previous iteration of the model version used here but comparing different complexities of the marine iron configurations (Yao et al., 2019) as well as other inverse modeling studies (Pasquier & Holzer, 2017, 2018). However, it must be noted that all of these model studies, including this one, only evaluated steady-state simulations in which uncertain parameters were manually tuned or optimized to best reproduce observations. Therefore, they are not necessarily indicative to how the iron dynamics in the model may respond to and impact marine productivity in externally forced transient scenarios.

There is a notable decrease in marine productivity and export production in the Southern Ocean among our model simulations with better representations of the global iron distribution (Table 3). The variable ligand parameterization predicts less ligands in the Southern Ocean (Figure 3), which allows higher scavenging to

reduce DFe that better reproduces observations. Furthermore, since external iron sources in the Southern Ocean are small (Figures 2 and 4m), the enhanced scavenging in the high source flux simulations removes more DFe than source fluxes add to the Southern Ocean. Therefore, DFe levels further decrease in the Southern Ocean (Figures 4o and 6) in the high source flux scenarios. The high scavenging in our best model simulation with variable ligands and high source fluxes (*Atm + SedHigh_LigVar*) reduces DFe, marine productivity and resulting oxygen consumption during remineralization of POM, thereby increasing dissolved oxygen concentrations at depth. This effect is significant enough to increase average global dissolved oxygen concentrations by 8% in the model because water masses formed in the Southern Ocean contribute to much of the global deep ocean (Table 3). This emphasizes the importance of simulating a robust global marine iron cycle most importantly in the Southern Ocean.

5. Conclusions

In this study we tested various rates of atmospheric soluble deposition, reductive sedimentary release, and variable ligand distributions within a marine iron component in a global ocean biogeochemical model. The simulations that best reproduce the global DFe observations include highest tested source fluxes and a variable ligand parameterization. The most striking feature in the global DFe observations that supports this hypothesis is the strong gradients that often occur with high concentrations near source fluxes and low concentrations in adjacent open ocean regions. This high source flux/scavenging iron cycling regime causes a relatively short residence times of less than a decade in the global oceans and less than a year in the surface ocean. The short residence time implies that the global marine iron cycle is highly sensitive to environmental perturbations in the Anthropocene and geological past. Uncertainties remain high due to model parameterizations of complex, poorly understood, and often intertwined processes (e.g., ligand production and subsequent control on scavenging near source inputs) and the sparsity of DFe and ligand measurements throughout the global ocean. Nevertheless, our model-data analysis suggests the marine iron cycle operates with high global source inputs and scavenging rates and low residence times compare to most previous estimates.

Data Availability Statement

Model code and output will be made publicly accessible at GEOMAR open access repository (https://thredds.geomar.de).

References

Anderson, R. F., Cheng, H., Edwards, R. L., Fleisher, M. Q., Hayes, C. T., Huang, K. F., et al. (2016). How well can we quantify dust deposition to the ocean? *Philosophical Transactions of The Royal Society A Mathematical Physical and Engineering Sciences*, *374*, 20150285. https://doi.org/10.1098/rsta.2015.0285

Aumont, O., Ethé, C., Tagliabue, A., Bopp, L., & Gehlen, M. (2015). PISCES-v2: An ocean biogeochemical model for carbon and ecosystem studies. *Geoscientific Model Development*, *8*, 2465–2513. https://doi.org/10.5194/gmd-8-2465-2015

Black, E. E., Kienast, S. S., Lemaitre, N., Lam, P. J., Anderson, R. F., Planquette, H., et al. (2020). Ironing out Fe residence time in the dynamic upper ocean. *Global Biogeochemical Cycles*, *34*. https://doi.org/10.1029/2020gb006592

Boyd, P. W., & Ellwood, M. J. (2010). The biogeochemical cycle of iron in the ocean. *Nature Geoscience*, *3*, 675–682. https://doi.org/10.1038/ngeo964

Bruland, K. W., Middag, R., & Lohan, M. C. (2014). 8.2 - Controls of trace metals in seawater. In H. D. Holland, & K. K. Turekian (Eds.), *Treatise on geochemistry* (2nd ed., pp. 19–51). Elsevier. https://doi.org/10.1016/B978-0-08-095975-7.00602-1

Bundy, R. M., Boiteau, R. M., McLean, C., Turk-Kubo, K. A., McIlvin, M. R., Saito, M. A., et al. (2018). Distinct siderophores contribute to iron cycling in the mesopelagic at station ALOHA. *Frontiers in Marine Science*, *5*. https://doi.org/10.3389/fmars.2018.00061

Conway, T. M., & John, S. G. (2014). Quantification of dissolved iron sources to the North Atlantic Ocean. *Nature*, *511*, 212–215. https://doi.org/10.1038/nature13482

Croot, P. L., Streu, P., & Baker, A. R. (2004). Short residence time for iron in surface seawater impacted by atmospheric dry deposition from Saharan dust events. *Geophysical Research Letters*, *31*. https://doi.org/10.1029/2004gl020153

Dale, A. W., Nickelsen, L., Scholz, F., Hensen, C., Oschlies, A., & Wallmann, K. (2015). A revised global estimate of dissolved iron fluxes from marine sediments. *Global Biogeochemical Cycles*, *29*, 691–707. https://doi.org/10.1002/2014gb005017

Eby, M., Zickfeld, K., Montenegro, A., Archer, D., Meissner, K. J., & Weaver, A. J. (2009). Lifetime of anthropogenic climate change: Millennial time scales of potential CO_2 and surface temperature perturbations. *Journal of Climate*, *22*, 2501–2511. https://doi.org/10.1175/2008jcli2554.1

Elrod, V. A., Berelson, W. M., Coale, K. H., & Johnson, K. S. (2004). The flux of iron from continental shelf sediments: A missing source for global budgets. *Geophysical Research Letters*, *31*, L12307. https://doi.org/10.1029/2004gl020216

Frants, M., Holzer, M., DeVries, T., & Matear, R. (2016). Constraints on the global marine iron cycle from a simple inverse model. *Journal of Geophysical Research: Biogeosciences*, *121*, 28–51. https://doi.org/10.1002/2015jg003111

Galbraith, E. D., Gnanadesikan, A., Dunne, J. P., & Hiscock, M. R. (2010). Regional impacts of iron-light colimitation in a global biogeochemical model. *Biogeosciences*, *7*, 1043–1064. https://doi.org/10.5194/bg-7-1043-2010

Gent, P. R., & McWilliams, J. C. (1990). Isopycnal Mixing in Ocean Circulation Models. *Journal of Physical Oceanography*, *20*, 150–155. https://doi.org/10.1175/1520-0485(1990)020<0150:IMIOCM>2.0.CO;2

Getzlaff, J., & Dietze, H. (2013). Effects of increased isopycnal diffusivity mimicking the unresolved equatorial intermediate current system in an earth system climate model. *Geophysical Research Letters*, *40*, 2166–2170. https://doi.org/10.1002/grl.50419

Gledhill, M., & Buck, K. N. (2012). The organic complexation of iron in the marine environment: A review. *Frontiers in Microbiology*, *3*. https://doi.org/10.3389/fmicb.2012.00069

Holzer, M., Frants, M., & Pasquier, B. (2016). The age of iron and iron source attribution in the ocean. *Global Biogeochemical Cycles*, *30*, 1454–1474. https://doi.org/10.1002/2016gb005418

Homoky, W. B., Conway, T. M., John, S. G., König, D., Deng, F., Tagliabue, A., & Mills, R. A. (2021). Iron colloids dominate sedimentary supply to the ocean interior. *Proceedings of the National Academy of Sciences*, *118*(13), e20160781.

Homoky, W. B., John, S. G., Conway, T. M., & Mills, R. A. (2013). Distinct iron isotopic signatures and supply from marine sediment dissolution. *Nature Communications*, *4*, 2143. https://doi.org/10.1038/ncomms3143

Honeyman, B. D., Balistrieri, L. S., & Murray, J. W. (1988). Oceanic trace metal scavenging: The importance of particle concentration, deep sea research part A. *Oceanographic Research Papers*, *35*, 227–246. https://doi.org/10.1016/0198-0149(88)90038-6

Johnson, K. S., Gordon, R. M., & Coale, K. H. (1997). What controls dissolved iron concentrations in the world ocean? *Marine Chemistry*, *57*, 137–161. https://doi.org/10.1016/S0304-4203(97)00043-1

Kalnay, E., Kanamitsu, M., Kistler, R., Collins, W., Deaven, D., Gandin, L., et al. (1996). The NCEP/NCAR 40-year reanalysis project. *Bulletin of the American Meteorological Society*, *77*, 437–471. https://doi.org/10.1175/1520-0477(1996)077<0437:tnyrp>2.0.co;2

Kessler, W. S., & McCreary, J. P. (1993). The annual wind-driven Rossby wave in the subthermocline equatorial Pacific. *Journal of Physical Oceanography*, *23*, 1192–1207. https://doi.org/10.1175/1520-0485(1993)023<1192:tawdrw>2.0.co;2

Kvale, K. F., Meissner, K. J., Keller, D. P., Eby, M., & Schmittner, A. (2015). Explicit planktic calcifiers in the University of Victoria Earth System Climate Model, Version 2.9. *Atmosphere-Ocean*, *53*, 332–350. https://doi.org/10.1080/07055900.2015.1049112

Large, W. G., Danabasoglu, G., McWilliams, J. C., Gent, P. R., & Bryan, F. O. (2001). Equatorial circulation of a global ocean climate model with anisotropic horizontal viscosity. *Journal of Physical Oceanography*, *31*, 518–536. https://doi.org/10.1175/1520-0485(2001)031<0518:ECOAGO>2.0.CO;2

Luo, C., Mahowald, N., Bond, T., Chuang, P. Y., Artaxo, P., Siefert, R., et al. (2008). Combustion iron distribution and deposition. *Global Biogeochemical Cycles*, *22*, GB1012. https://doi.org/10.1029/2007gb002964

Misumi, K., Lindsay, K., Moore, J. K., Doney, S. C., Tsumune, D., & Yoshida, Y. (2013). Humic substances may control dissolved iron distributions in the global ocean: Implications from numerical simulations. *Global Biogeochemical Cycles*, *27*, 450–462. https://doi.org/10.1002/gbc.20039

Moffett, J. W., Goepfert, T. J., & Naqvi, S. W. A. (2007). Reduced iron associated with secondary nitrite maxima in the Arabian Sea. *Deep Sea Research Part I: Oceanographic Research Papers*, *54*, 1341–1349. https://doi.org/10.1016/j.dsr.2007.04.004

Moore, C. M., Mills, M. M., Arrigo, K. R., Berman-Frank, I., Bopp, L., Boyd, P. W., et al. (2013). Processes and patterns of oceanic nutrient limitation. *Nature Geoscience*, *6*, 701–710. https://doi.org/10.1038/ngeo1765

Moore, J. K., & Braucher, O. (2008). Sedimentary and mineral dust sources of dissolved iron to the world ocean. *Biogeosciences*, *5*, 631–656. https://doi.org/10.5194/bg-5-631-2008

Muglia, J., Somes, C. J., Nickelsen, L., & Schmittner, A. (2017). Combined Effects of Atmospheric and Seafloor Iron Fluxes to the Glacial Ocean. *Paleoceanography*, *32*, 1204–1218. https://doi.org/10.1002/2016pa003077

Myriokefalitakis, S., Ito, A., Kanakidou, M., Nenes, A., Krol, M. C., Mahowald, N. M., et al. (2018). Reviews and syntheses: The GESAMP atmospheric iron deposition model intercomparison study. *Biogeosciences*, *15*, 6659–6684. https://doi.org/10.5194/bg-15-6659-2018

Nickelsen, L., Keller, D. P., & Oschlies, A. (2015). A dynamic marine iron cycle module coupled to the University of Victoria Earth System Model: The Kiel Marine Biogeochemical Model 2 for UVic 2.9. *Geoscientific Model Development*, *8*, 1357–1381. https://doi.org/10.5194/gmd-8-1357-2015

Parekh, P., Follows, M. J., & Boyle, E. (2004). Modeling the global ocean iron cycle. *Global Biogeochemical Cycles*, *18*. https://doi.org/10.1029/2003gb002061

Pasquier, B., & Holzer, M. (2017). Inverse-model estimates of the ocean's coupled phosphorus, silicon, and iron cycles. *Biogeosciences*, *14*, 4125–4159. https://doi.org/10.5194/bg-14-4125-2017

Pasquier, B., & Holzer, M. (2018). The number of past and future regenerations of iron in the ocean and its intrinsic fertilization efficiency. *Biogeosciences*, *15*, 7177–7203. https://doi.org/10.5194/bg-15-7177-2018

Peltier, W. R. (2004). Global glacial isostasy and the surface of the ice-age Earth: The ICE-5G (VM2) model and GRACE. *Annual Review of Earth and Planetary Sciences*, *32*, 111–149. https://doi.org/10.1146/annurev.earth.32.082503.144359

Pham, A. L. D., & Ito, T. (2018). Formation and maintenance of the GEOTRACES subsurface-dissolved iron maxima in an ocean biogeochemistry model. *Global Biogeochemical Cycles*, *32*, 932–953. https://doi.org/10.1029/2017gb005852

Pham, A. L. D., & Ito, T. (2019). Ligand binding strength explains the distribution of iron in the North Atlantic Ocean. *Geophysical Research Letters*, *46*, 7500–7508. https://doi.org/10.1029/2019gl083319

Resing, J. A., Sedwick, P. N., German, C. R., Jenkins, W. J., Moffett, J. W., Sohst, B. M., & Tagliabue, A. (2015). Basin-scale transport of hydrothermal dissolved metals across the South Pacific Ocean. *Nature*, *523*, 200–203. https://doi.org/10.1038/nature14577

Roshan, S., DeVries, T., Wu, J., John, S., & Weber, T. (2020). Reversible scavenging traps hydrothermal iron in the deep ocean. *Earth and Planetary Science Letters*, *542*, 116297. https://doi.org/10.1016/j.epsl.2020.116297

Sarthou, G., Baker, A. R., Blain, S., Achterberg, E. P., Boye, M., Bowie, A. R., et al. (2003). Atmospheric iron deposition and sea-surface dissolved iron concentrations in the eastern Atlantic Ocean. *Deep Sea Research Part I: Oceanographic Research Papers*, *50*, 1339–1352. https://doi.org/10.1016/S0967-0637(03)00126-2

Schlitzer, R., Anderson, R. F., Dodas, E. M., Lohan, M., Geibert, W., Tagliabue, A., et al. (2018). The GEOTRACES Intermediate Data Product 2017. *Chemical Geology*, *493*, 210–223. https://doi.org/10.1016/j.chemgeo.2018.05.040

Schmittner, A., & Egbert, G. D. (2014). An improved parameterization of tidal mixing for ocean models. *Geoscientific Model Development*, *7*, 211–224. https://doi.org/10.5194/gmd-7-211-2014

Schmittner, A., & Somes, C. J. (2016). Complementary constraints from carbon (^{13}C) and nitrogen (^{15}N) isotopes on the glacial ocean's soft-tissue biological pump. *Paleoceanography*, *31*, 669–693. https://doi.org/10.1002/2015PA002905

Somes, C., Schmittner, A., Muglia, J., & Oschlies, A. (2017). A three-dimensional model of the marine nitrogen cycle during the Last Glacial Maximum constrained by sedimentary isotopes. *Frontiers in Marine Science*, *4*. https://doi.org/10.3389/fmars.2017.00108

Somes, C. J., & Oschlies, A. (2015). On the influence of "non-Redfield" dissolved organic nutrient dynamics on the spatial distribution of N2 fixation and the size of the marine fixed nitrogen inventory. *Global Biogeochemical Cycles*, *29*, 973–993. https://doi.org/10.1002/2014GB005050

Somes, C. J., Schmittner, A., Galbraith, E. D., Lehmann, M. F., Altabet, M. A., Montoya, J. P., et al. (2010). Simulating the global distribution of nitrogen isotopes in the ocean. *Global Biogeochemical Cycles*, *24*, GB4019. https://doi.org/10.1029/2009gb003767

Tagliabue, A., Aumont, O., DeAth, R., Dunne, J. P., Dutkiewicz, S., Galbraith, E., et al. (2016). How well do global ocean biogeochemistry models simulate dissolved iron distributions? *Global Biogeochemical Cycles*, *30*, 149–174. https://doi.org/10.1002/2015gb005289

Tagliabue, A., Bopp, L., Dutay, J.-C., Bowie, A. R., Chever, F., Jean-Baptiste, P., et al. (2010). Hydrothermal contribution to the oceanic dissolved iron inventory. *Nature Geoscience*, *3*, 252–256. https://doi.org/10.1038/ngeo818

Tagliabue, A., Bowie, A. R., Boyd, P. W., Buck, K. N., Johnson, K. S., & Saito, M. A. (2017). The integral role of iron in ocean biogeochemistry. *Nature*, *543*, 51–59. https://doi.org/10.1038/nature21058

Tagliabue, A., Bowie, A. R., DeVries, T., Ellwood, M. J., Landing, W. M., Milne, A., et al. (2019). The interplay between regeneration and scavenging fluxes drives ocean iron cycling. *Nature Communications*, *10*. https://doi.org/10.1038/s41467-019-12775-5

Tagliabue, A., Mtshali, T., Aumont, O., Bowie, A. R., Klunder, M. B., Roychoudhury, A. N., & Swart, S. (2012). A global compilation of dissolved iron measurements: Focus on distributions and processes in the Southern Ocean. *Biogeosciences*, *9*, 2333–2349. https://doi.org/10.5194/bg-9-2333-2012

Tagliabue, A., & Völker, C. (2011). Toward accounting for dissolved iron speciation in global ocean models. *Biogeosciences*, *8*, 3025–3039. https://doi.org/10.5194/bg-8-3025-2011

Völker, C., & Tagliabue, A. (2015). Modeling organic iron-binding ligands in a three-dimensional biogeochemical ocean model. *Marine Chemistry*, *173*, 67–77. https://doi.org/10.1016/j.marchem.2014.11.008

Weaver, A. J., Eby, M., Wiebe, E. C., Bitz, C. M., Duffy, P. B., Ewen, T. L., et al. (2001). The UVic earth system climate model: Model description, climatology, and applications to past, present and future climates. *Atmosphere-Ocean*, *39*, 361–428. https://doi.org/10.1080/07055900.2001.9649686

Yao, W., Kvale, K. F., Achterberg, E., Koeve, W., & Oschlies, A. (2019). Hierarchy of calibrated global models reveals improved distributions and fluxes of biogeochemical tracers in models with explicit representation of iron. *Environmental Research Letters*, *14*, 114009. https://doi.org/10.1088/1748-9326/ab4c52

Ye, Y., & Völker, C. (2017). On the role of dust-deposited lithogenic particles for iron cycling in the tropical and subtropical Atlantic. *Global Biogeochemical Cycles*, *31*, 1543–1558. https://doi.org/10.1002/2017gb005663